# An Efficient Forward Solver in Electrical Impedance Tomography by Spectral Element Method

Kim Hwa Lim, Joon-Ho Lee, Gang Ye, and Qing Huo Liu*, *Fellow, IEEE*

***Abstract*—In electrical impedance tomography (EIT), a forward solver capable of predicting the voltages on electrodes for a given conductivity distribution is essential for reconstruction. The EIT forward solver is normally based on the conventional finite element method (FEM). One of the major problems of three-dimensional (3-D) EIT is its high demand in computing power and memory since high precision is required for obtaining a small secondary field which is typical for a small anomaly. This accuracy requirement is also set by the level of noise in the real data; although currently the noise level is still an issue, future EIT systems should significantly reduce the noise level to be capable of detecting very small anomalies. To accurately simulate the forward solution with the FEM, a mesh with large number of nodes and elements is usually needed. To overcome this problem, we proposed the spectral element method (SEM) for EIT forward problem. With the introduction of SEM, a smaller number of nodes and hence less computational time and memory are needed to achieve the same or better accuracy in the forward solution than the FEM. Numerical results demonstrate the efficiency of the SEM in 3-D EIT simulation.**

***Index Terms*—Electrical impedance tomography (EIT), finite element method (FEM), forward solver, spectral element method (SEM).**

## I. Introduction

THE basic idea of electrical impedance tomography (EIT) is to reconstruct the internal electrical conductivity distribution of the medium by measuring the low-frequency electrical potentials on the boundary. To measure the surface potentials, an array of electrodes is attached to the boundary. A set of current patterns is applied to the electrodes and the voltages on the probing electrodes are measured. From these measured voltages, the internal electrical properties, namely conductivity or admittivity, can be estimated. The three major applications of EIT are biomedical imaging [1]–[5], geophysical exploration [6], [7], and industrial applications [8]–[11].

A forward solver capable of predicting the voltages on electrodes for a given conductivity distribution is essential for EIT reconstruction. One of the most popular reconstruction algorithms is the regularized Gauss–Newton or quasi-Newton method [4], [7], [12]. In each of the Newton iterations, the forward solver will be called to compute the voltages on the electrodes and the internal electric potential, as well as the Fréchet derivatives. The internal electric potential is required to assemble the Jacobian matrix for the inversion, for details please refer to [4], [13]. So it is a prerequisite to have a forward solver capable of predicting the voltages at least as accurately as the measured data.

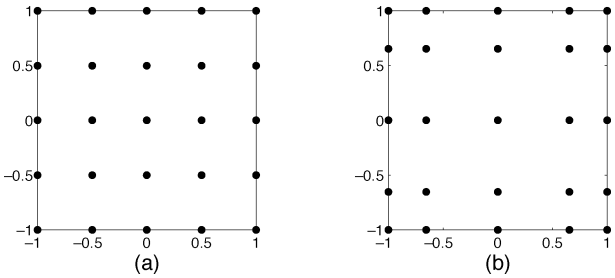


Fig. 1. Nodal distribution in 2-D for fourth order (a) FEM and (b) SEM.

The forward solver is normally based on the first order finite element method (FEM) with the complete electrode model (CEM) [4], [14]–[16]. Here, we refer the first order FEM as the conventional FEM. It has been noted that the complete electrode model is superior to the previous continuum, gap and shunt models because it predicts the measured data more accurately [16], [17]. One of the problems of three-dimensional (3-D) EIT is its high demand on computing power and memory. This is because the total number of unknowns becomes exceedingly large if we need to accurately simulate the forward solution for a small object. The secondary field (i.e., the difference in the potential between the medium with and without the object) of a small object is a few order smaller than the primary field (i.e., the potential for the background). One of the ways to reduce the numerical error is to refine the mesh adaptively where the solution is most likely to suffer from discretization errors. As the electric field is more intense near the electrodes, a finer mesh will be needed in these areas. Consequently, the mesh of a 3-D EIT system with more than 64 electrodes will require a large number of nodes. It is, thus, desirable to have a method that is able to achieve the same accuracy as the conventional FEM forward solver with fewer nodes and elements.

One of the immediate candidates is the higher-order FEM. In the higher-order FEM, the basis functions are higher order Lagrange polynomials passing through regular uniform grid points in each volume element. It is able to achieve better accuracy than the conventional FEM. In this paper, we propose to use the spectral element method (SEM) for EIT forward problem. The SEM is capable of achieving even better accuracy than higher order FEM because of the distribution of nodal points. The nodal distributions of a high-order FEM and SEM in two-dimensional (2-D) are shown in Fig. 1.

Manuscript received February 15, 2006; revised March 28, 2006. This work was supported by the Susan Komen Breast Cancer Foundation under Grant IMG02-1054-3-D. *Asterisk indicates corresponding author.*

K. H. Lim, J.-H. Lee, and G. Ye are with Department of Electrical and Computer Engineering, Duke University, Durham, NC 27708-0291 USA.

*Q. H. Liu is with Department of Electrical and Computer Engineering, Duke University, Durham, NC 27708-0291 USA (e-mail: qhliu@ee.duke.edu).

Digital Object Identifier 10.1109/TMI.2006.876143

The SEM was first proposed in 1984 by Patera *et al.* in computational fluid dynamics [18]. It has the flexibility of the FEM and the high accuracy of the spectral and pseudospectral methods. The SEM is basically a higher-order FEM, with the major difference in their basis functions. The basis functions of SEM are based on Gauss–Lobatto–Legendre (GLL) points in which the functions are Lagrange polynomials passing through these GLL points, whereas the FEM basis functions are based on uniform grid points in the reference domain. These basis functions are orthogonal to one another in both FEM and SEM. However, the SEM is more accurate than higher order FEM because interpolation by GLL nodes is able to suppress the so-called Runge Phenomenon [19] in the FEM. Note the Runge phenomenon is the high interpolation error near the boundaries when high-order polynomial interpolation is used with uniform nodal points, as in the higher order FEM. Another characteristic of SEM is that can achieve the so-called *Spectral Accuracy* in which the error decreases exponentially with the order of the basis functions [19]–[23]. To evaluate integrals in each components of the system matrix, the GLL quadrature integration can be easily employed. This has rendered SEM much easier to implement than the higher order FEM, although the latter can also be achieved by the same numerical quadrature. In this paper, due to the lacking of higher order FEM codes, we compare the results of SEM to the first-order FEM which is the conventional FEM.

The organization of the paper is as follows. In Section II, we will present the detail formulations of the EIT forward problem and the SEM. This will be followed by the numerical results for the SEM and its comparison with conventional FEM and experimental data in Section III. Finally, we will have concluding remarks in Section IV.

## II. Formulation

### A. The EIT Forward Problem

EIT problem is schematically shown in Fig. 2. The system consists of a number of source and probing electrodes. The forward problem of EIT can be described by Laplace's equation

$$\nabla \cdot \sigma \nabla u(\mathbf{r}) = 0, \qquad \mathbf{r} \in \Gamma \tag{1}$$

where $\Gamma$ is the imaging domain and $\partial\Gamma$ is its outer boundary. The electrical potential and conductivity distribution in $\Gamma$ are denoted as $u(\mathbf{r})$ and $\sigma(\mathbf{r})$, respectively.

The boundary conditions that we used are the mixed boundary conditions (Dirichlet and Neumann) which are based on the so called the complete electrode model [4]: If $I_l$ is the current injected from the $l$th electrode $E_l$ with a contact impedance $Z_l$, the boundary conditions on this electrode are

$$V_l = u + Z_l \sigma \frac{\partial u}{\partial n} \tag{2}$$

$$I_l = \int_{E_l} \sigma \frac{\partial u}{\partial n} dS \tag{3}$$

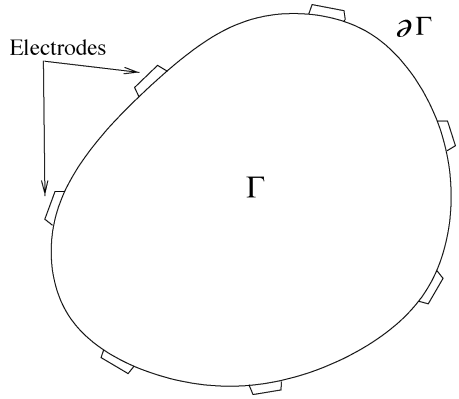


Fig. 2. Schematic diagram of EIT system.

where $V_l$ is the voltage measured on electrode $E_l$, $\hat{n}$ is the outward unit normal vector, and $\sigma(\partial u/\partial n)$ is the inward current density on the surface boundary. The boundary condition on the inter electrodes gap is simply

$$\sigma \frac{\partial u}{\partial n} = 0. \tag{4}$$

In order to make sure that the model has a unique solution, charge conservation

$$\sum_{l=1}^{L} I_l = 0 \tag{5}$$

must be satisfied, and a choice of ground condition needs to be set. The grounding condition that we used is simply $V_g = 0$ where $g$th electrode is the ground electrode.

### B. Galerkin's Formulation

The conventional way of solving the EIT forward problem is the FEM. The detail formulation of FEM for EIT with complete electrode model can be found in [4], [17]. In the SEM, a similar Galerkin's formulation is used.

From the Laplace's equation (1), we form the weak form equation by testing function $\{\phi_i\}$

$$\int_{\Gamma} \phi_i \nabla \cdot \sigma \nabla u dV = 0. \tag{6}$$

Here, the testing functions $\{\phi_i\}$ are chosen the same as the basis functions in this Galerkin's formulation. In the conventional FEM, these are just linear shape functions peak at the nodal points of each volume element.

Next, we expand $u$ in terms of the basis functions $\{\phi_j\}$, i.e. $u = \sum_j u_j \phi_j$ and substitute it into (6)

$$\sum_j u_j \int_{\Gamma} \phi_i \nabla \cdot \sigma \nabla \phi_j dV = 0 \tag{7}$$

and after integration by parts we arrive at

$$\sum_j u_j \int_\Gamma \sigma \nabla \phi_i \cdot \nabla \phi_j dV = \int_{\partial\Gamma} \phi_i \sigma \frac{\partial u}{\partial n} ds. \tag{8}$$

From (2), the current density can be rearranged as

$$\sigma \frac{\partial u}{\partial n} = \frac{1}{Z_l} \left( V_l - \sum_j u_j \phi_j \right) \tag{9}$$

on the electrodes.

Substituting this into (8), we arrive at

$$\sum_j u_j \int_\Gamma \sigma \nabla \phi_i \cdot \nabla \phi_j dV = \int_{\partial\Gamma} \phi_i \frac{1}{Z_l} \left( V_l - \sum_j u_j \phi_j \right) ds \tag{10}$$

with $i, j = 1, \ldots, N_n$ and $N_n$ is the number of nodes. Equation (10) can be written in matrix form

$$\begin{bmatrix} A & B \\ B^T & C \end{bmatrix} \begin{bmatrix} U \\ V_L \end{bmatrix} = \begin{bmatrix} 0 \\ I \end{bmatrix}. \tag{11}$$

Here, $U, V_L$, and $I$ are column vectors formed by $\{u_i\}, \{V_l\}$ and $\{I_l\}$, respectively, with indices $i = 1, \ldots, N_n$ and $l = 1, \ldots, L$. Each of the elemental matrices $A$, $B$ and $C$, denoted as $A_e$, $B_e$, and $C_e$ are given by

$$A_e(i,j) = \int_\Gamma \sigma \nabla \phi_i \cdot \nabla \phi_j dV + \int_{\partial\Gamma} \frac{1}{Z_l} \phi_i \phi_j ds \tag{12}$$

$$B_e(i,j) = -\int_{E_l} \frac{1}{Z_l}_j \phi_i ds \tag{13}$$

$$C_e(i,l) = \frac{1}{Z_l} |E_l| \qquad \text{for} \qquad i = l \tag{14}$$

where indices $i = 1, \ldots, N_n$ and $l = 1, \ldots, L$. Here, $|E_l|$ is the area of the $l$th electrode.

The matrix formed by the elemental matrices $A_e$, $B_e$, and $C_e$

$$S = \sum_{e=1}^{N_e} \begin{bmatrix} A_e & B_e \\ B_e^T & C_e \end{bmatrix} \tag{15}$$

is known as the global admittance matrix, where $N_e$ is the number of elements. The admittance matrix is, however, not in full-rank and therefore the system equation (11) does not have a unique solution. In order to overcome this, a choice of grounding condition needs to be made. In this paper, we achieve the grounding condition by taking away the row and column of the admittance matrix which correspond to a fixed ground electrode and then set the corresponding $V_g = 0$.

### C. Basis Functions for SEM

The SEM is basically the same as the higher-order FEM except for the basis functions and their integration method. The basis functions of a higher order FEM are polynomials passing through regular grid points. However, the SEM is based on GLL points in which its basis functions are polynomials passing through these GLL points.

The $N$th order GLL basis functions in a one-dimensional standard reference element $\xi \in [-1, 1]$ are defined by

$$\phi_j^{(N)}(\xi) = \frac{-1}{N(N+1)L_N(\xi_j)} \frac{(1-\xi^2)L_N'(\xi)}{(\xi - \xi_j)} \tag{16}$$

for $j = 0, \ldots, N$, where $L_N(\xi)$ is the Legendre polynomial of $N$th order and $L_N'(\xi)$ is its derivative. The grid points $\xi_j$, $j = 0, 1, \ldots, N$ within the element $\xi \in [-1, 1]$ are chosen as the GLL points, i.e., the zeros of $(1-\xi^2)L_N'(\xi)$. Using (16) as the basis functions, an arbitrary smooth function can be interpolated as

$$f(\xi) \cong \sum_{j=0}^{N} f(\xi_j) \phi_j^{(N)}(\xi) \tag{17}$$

with an error of $O(\Delta\xi^{N+1})$, where $\Delta\xi$ is the average increment of the grid points [20]. By definition, the above Lagrange–Legendre interpolation has a property

$$\phi_j^{(N)}(\xi_i) = \delta_{ji}. \tag{18}$$

The integration of a function can be performed numerically by the GLL quadrature

$$\int_{-1}^{1} f(\xi) d\xi = \sum_{j=0}^{N} w_j^{(N)} f(\xi_j) \tag{19}$$

with an error of $O(\Delta\xi^{2N})$ [20], where the GLL quadrature weights for the numerical integration are

$$w_j^{(N)} = \frac{2}{N(N+1)L_N^2(\xi_j)}. \tag{20}$$

In 3-D, within the standard reference element, i.e., a cubic element $(\xi, \eta, \zeta) \in [-1, 1] \times [-1, 1] \times [-1, 1]$, the basis functions can be written as

$$\phi_{\text{rst}}(\xi, \eta, \zeta) = \phi_r^{(N)}(\xi) \phi_s^{(N)}(\eta) \phi_t^{(N)}(\zeta) \tag{21}$$

for $r = 0, \ldots, N$; $s = 0, \ldots, N$; $t = 0, \ldots, N$. With these basis functions, an arbitrary 3-D function $f(\xi, \eta, \zeta)$ can be written as

$$f(\xi, \eta, \zeta) \cong \sum_{r=0}^{N} \sum_{s=0}^{N} \sum_{t=0}^{N} f(\xi_r, \eta_s, \zeta_t) \phi_{rst}(\xi, \eta, \zeta). \tag{22}$$

The integration of a function becomes

$$\int_{-1}^{1} \int_{-1}^{1} \int_{-1}^{1} f(\xi, \eta, \zeta) d\xi d\eta d\zeta \cong \sum_{r=0}^{N} \sum_{s=0}^{N} \sum_{t=0}^{N} w_r^{(N)} w_s^{(N)} w_t^{(N)} f(\xi_r, \eta_s, \zeta_t). \tag{23}$$

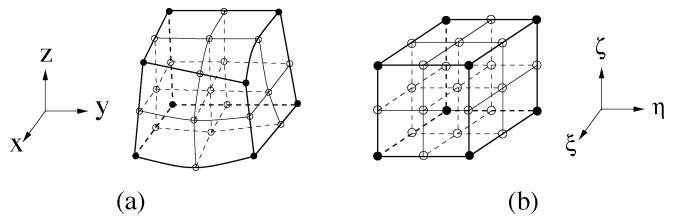


Fig. 3. General curved hexahedron in the (a) physical domain and (b) reference domain. Here only the second-order mapping is shown.

### *D. SEM for the EIT Forward Problem*

To apply the SEM to the EIT forward problem, the physical domain is first divided into hexahedral elements. Each of the hexahedral element in Cartesian coordinates $(x, y, z)$ is mapped into a local reference cubic element in $(\xi, \eta, \zeta)$ coordinates, see Fig. 3. The meshing with hexahedron elements is more difficult than tetrahedral meshing. One of the ways is to mesh it with tetrahedrons and then split each tetrahedron into four hexahedrons. The hexahedron meshing is still an ongoing research topic which deserves much attention.

The global admittance matrix $S$ in (15) is assembled by going through each hexahedral element and by computing the elemental matrices $A_e$, $B_e$, and $C_e$ in local reference coordinates. The first and second terms of $A_e$ in (12) computed in local coordinates become

$$\int_{\Gamma_e} \sigma \nabla \phi_i \cdot \nabla \phi_j dx dy dz = \int_{-1}^{1}\int_{-1}^{1}\int_{-1}^{1} \sigma \nabla_r \phi_i(\xi,\eta,\zeta) \cdot \mathbf{J}_e^{-T}\mathbf{J}_e^{-1}\nabla_r \phi_j(\xi,\eta,\zeta)|\mathbf{J}_e| d\xi d\eta d\zeta \quad (24)$$

and

$$\int_{\partial\Gamma} \frac{1}{Z_l}\phi_i(x,y,z)\phi_j(x,y,z)ds = \frac{1}{Z_l}\int_{-1}^{1}\int_{-1}^{1} \phi_i(\xi,\eta,\zeta)\phi_j(\xi,\eta,\zeta)|\mathbf{J}_b| du dv \quad (25)$$

where $\mathbf{J}_e$ is the Jacobian matrix associated with the mapping from a hexahedral element to the local reference cubic element, $\mathbf{J}_b$ is the Jacobian matrix associated with the mapping from a boundary surface element to the local reference surface element, and $(u, v)$ are the local reference coordinates on the boundary. Note that the boundary contribution in (25) is nonzero only for elements on the outer boundary $\partial\Gamma$.

The gradient $\nabla_r$ is defined as

$$\begin{aligned}\nabla_r \phi_i &= \nabla_r [\phi_r(\xi)\phi_s(\eta)\phi_t(\zeta)] \\ &= \hat{\boldsymbol{\xi}}\frac{d\phi_r(\xi)}{d\xi}\phi_s(\eta)\phi_t(\zeta) + \hat{\boldsymbol{\eta}}\phi_r(\xi)\frac{d\phi_s(\eta)}{d\eta}\phi_t(\zeta) \\ &\quad + \hat{\boldsymbol{\zeta}}\phi_r(\xi)\phi_s(\eta)\frac{d\phi_t(\zeta)}{d\zeta}. \end{aligned} \quad (26)$$

Component $B_e$ in (13) becomes

$$B_e(i,j) = -\frac{1}{Z_l}_j \int_{-1}^{1}\int_{-1}^{1} \phi_i(\xi,\eta,\zeta)|\mathbf{J}_b| du dv. \quad (27)$$

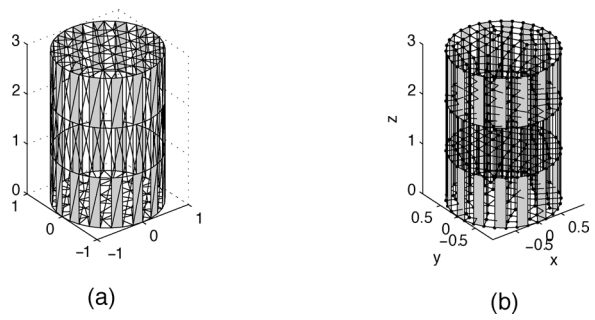


Fig. 4. (a) Tetrahedral mesh used in EIDORS. (b) Hexahedral mesh for SEM.

Component $C_e$ remains the same (14) as it can be computed directly with the physical values of electrodes. To compute (24), (25), and (27), numerical integration by quadrature described in (23) is employed. Once the global admittance $S$ has been assembled, (11) can be solved the same way as in FEM.

## III. Results and Discussions

### *A. Validation*

To validate the results of SEM, a cylindrical mesh with 32 electrodes, the same geometry as the demonstration case found in EIDORS 3-D toolkit [4], is used. The cylinder has a height of 3 m and radius of 1 m. It has two layers of 16 rectangular electrodes attached on its boundary as shown in Fig. 4. The mesh used in the EIDORS 3-D toolkit has 828 tetrahedral cells and 252 nodes, whereas our mesh for SEM has 255 hexahedral cells and 408 nodes.

In the simulation, the contact impedances of the electrodes are set to $Z_l = 0.001\ \Omega \cdot \mathrm{m}^2$. The current patterns used are the adjacent pair current patterns in which 16 pairs of horizontally adjacent electrodes from each planes are chosen to be source and ground. There are altogether 32 current patterns and each current pattern has 32 voltage measurements on the electrodes. Therefore, there will be $32 \times 32 = 1024$ voltage measurements.

To visualize the voltage on electrodes for all current patterns, we stack all the 1024 voltage values together. In Fig. 5, the first 256 normalized voltage values for SEM and EIDORS results are shown. The normalized voltage is obtained by dividing the voltage on an electrode by the maximum value of all the voltages that belong to the same current pattern.

The result for SEM is obtained using the first order GLL basis functions, the same order as in the conventional FEM. The results show that the two methods agree very well with the $L_2$ norm error less than 0.001. However, if we use the absolute instead of the normalized voltage value, the error will be much larger. This is because both our SEM and EIDORS results have not converged to the exact solution yet with this mesh. To obtain a more accurate solution, we need to use either a much denser mesh or higher-order elements in FEM or SEM. One way is to refine the mesh adaptively where the solution is most likely to suffer from discretization errors [17]. As the electric potential changes more rapidly near the electrodes, a finer mesh will be needed in these areas. A 3-D EIT system with the number of electrodes exceeding 64 will require a large number of nodes. It is thus desirable to have a method that is able to achieve the

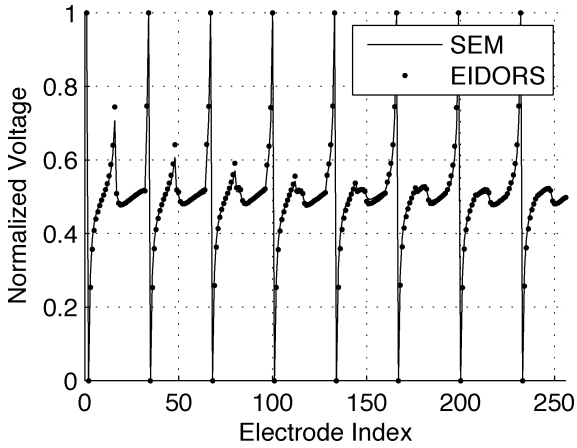


Fig. 5. Normalized voltage measurements. There are altogether 1024 voltage measurements, here only the first 256 are plotted. The normalized voltage is obtained by dividing the voltage on an electrode by the maximum value of all the voltages that belong to the same current pattern.

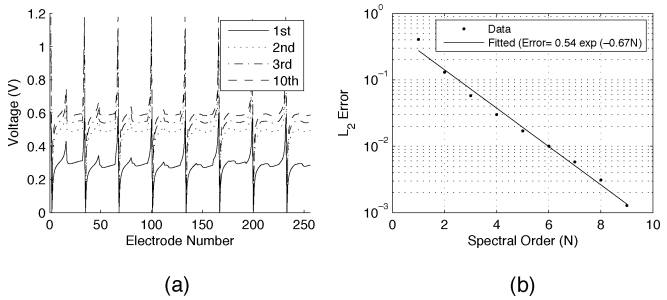


Fig. 6. Higher order SEM results with $Z_l = 0.001\ \Omega \cdot \mathrm{m}^2$. (a) First, second, third, and tenth order. (b) Error convergence.

same accuracy as the conventional FEM forward solver with fewer nodes and elements. The higher-order SEM is an ideal candidate for this requirement. In the next subsection, we shall study the performance of the higher-order SEM with the same geometry as described here.

### B. Higher Order SEM Results

*1) Spectral Convergence of SEM:* The first example of a higher order SEM is shown in Fig. 6(a). The result is obtained using the mesh in Fig. 4(b) and a contact impedance $Z_l = 0.001\ \Omega \cdot \mathrm{m}^2$. As before, only the first 256 out of 1024 values are plotted. Here, we only show the first-, second-, third-, and tenth-order results.

The tenth-order result is the most accurate solution which we can safely take it as the reference solution. From the graph in Fig. 6(a), we observe that the result converges to the reference solution as the number of order increases. The error convergence for this result is shown in Fig. 6(b). The error is the $L_2$ norm error with the tenth order result as the reference. One of the characteristics of SEM is its spectral accuracy in which the error $\epsilon_N$ decreases exponentially with the increasing order $N$ [20], i.e.,

$$\epsilon_N \propto e^{-\beta N}, \qquad \beta > 0. \tag{28}$$

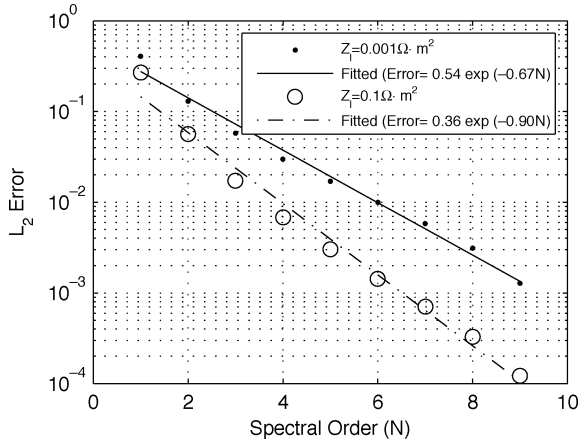


Fig. 7. Error convergence for $Z_l = 0.001\ \Omega \cdot \mathrm{m}^2$ and $Z_l = 0.1\ \Omega \cdot \mathrm{m}^2$.

The least square fitted line indeed shows that the error decreases exponentially with the exponent $\beta = 0.67$. Ideally, the exponent $\beta$ should as large as possible.

One possible reason why this $\beta$ is not very large may be the singularities in the current density near the edges of electrodes when there is no or relatively small contact impedance. According to [16] and [17], the current density peaks at the edges of the electrodes when the contact impedances are small. The contact impedance used in this example is only $0.001\ \Omega \cdot \mathrm{m}^2$ which is rather small and hence the problem of singularities.

To validate the above claim, we increase the contact impedance $Z_l$ to $0.1\ \Omega \cdot \mathrm{m}^2$. The error convergence for both $Z_l = 0.001\ \Omega \cdot \mathrm{m}^2$ and $Z_l = 0.1\ \Omega \cdot \mathrm{m}^2$ are shown in Fig. 7. Clearly, the overall performance for the $Z_l = 0.1\ \Omega \cdot \mathrm{m}^2$ case is better than that of $Z_l = 0.001\ \Omega \cdot \mathrm{m}^2$. The exponent $\beta$ becomes 0.9, much closer to the value of 1.

*2) Comparison Between SEM and FEM:* A numerical experiment is set up to compare the efficiency of SEM and conventional FEM. The geometry of the experiment is the same as the Section III-A. Two set of meshes, one for the FEM and one for the SEM are generated. The meshes for FEM will have the same number of nodes as the number of degrees of freedom of the higher order SEM. This is to show that with the same degrees of freedom, the SEM is able to achieve better accuracy than the FEM.

First of all, we found that the second-, third-, fourth-, and fifth-order SEM meshes have 2611, 8140, 18525, and 35296 degrees-of-freedom, respectively. Then, we refine the mesh in Fig. 4(b) so that they have the same number of nodes as the higher-order SEM. The refined meshes that correspond to the second and third order are shown in Fig. 8. We generated the refined meshes up to the fifth order.

We apply the conventional FEM to these refined meshes and the results are shown in Fig. 9. The machine that we used to run this case is a personal computer with 2.4-GHz Intel Pentium processor and 1 GB of RAM running on Linux operating system. In Fig. 9(a), the $L_2$ error versus the spectral order $N$ is shown. In Fig. 9(b), the $L_2$ error versus the number of nodes is shown. From these two figures, we observe that with the same number of nodes, the SEM can achieve a much smaller error than the conventional FEM. In order to achieve an accuracy of just 0.03,

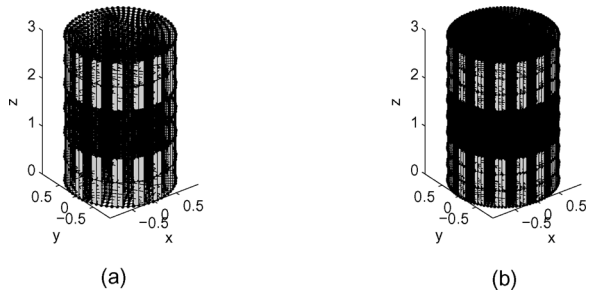


Fig. 8. Refined mesh with the same number of nodes as (a) second-order SEM and (b) third-order SEM.

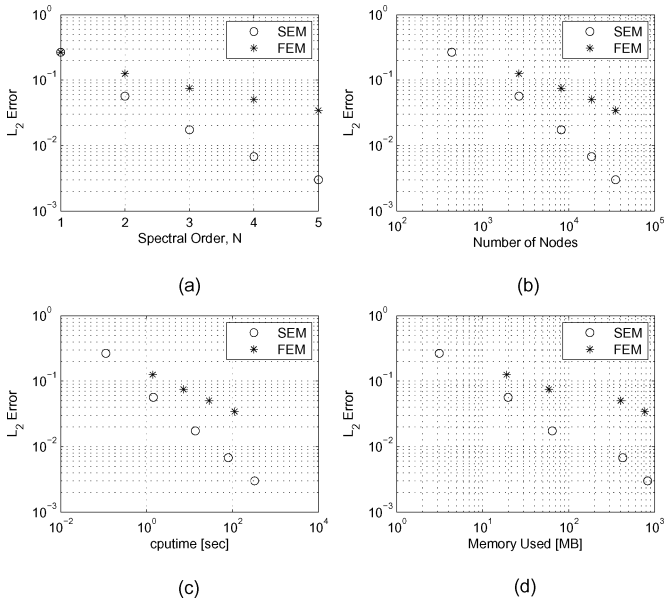


Fig. 9. (a) $L_2$ error versus spectral order. (b) $L_2$ error versus number of nodes. (c) $L_2$ error versus CPU times. (d) $L_2$ error versus memory.

the conventional FEM needs more than $3 \times 10^4$ nodes, but the SEM just needs $5 \times 10^3$ nodes.

In Fig. 9(c), the $L_2$ error versus CPU time is plotted. The CPU time is the total time taken to assemble the system matrix and also to solve the system equation. The preconditioned conjugate-gradient method is used to solve the system equation, where the preconditioner is the diagonal part of the system matrix. Given an accuracy of 0.03, the conventional FEM needs more than 100 s, whereas the SEM needs about 20 s, over five-fold improvement. Furthermore, from Fig. 9(d), we observe that the memory usage for the SEM is much less than that of conventional FEM. The memory usage is mainly for the storage of sparse system matrix. For the same accuracy of 0.03, conventional FEM has used more than 700 MB memory, but the SEM has used only 50 MB, more than ten times in memory saving. With these comparisons, the superiority of the SEM in terms of computational time and memory usage has been illustrated. The main reason for the EIT system to require very high accuracy is that the secondary field is usually several orders of magnitude smaller than the primary field. This will be further illustrated below.

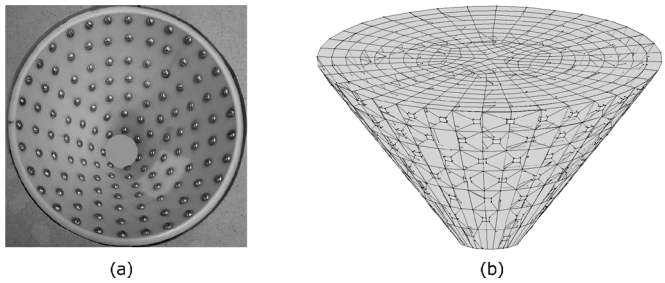


Fig. 10. (a) Funnel-shaped applicator with 128 electrodes attached to it. (b) Cone shape mesh used to simulate the applicator.

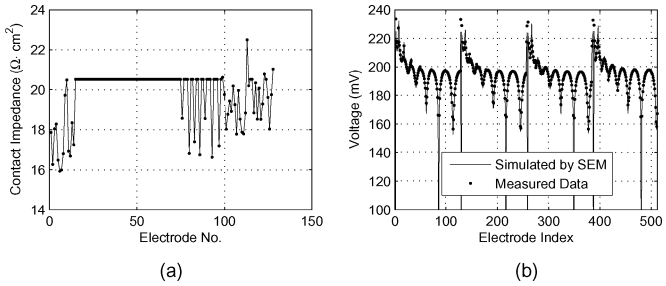


Fig. 11. (a) Contact impedances estimated for all the electrodes. Some of the values are constant because we do not have enough information to estimate them. (b) Simulated and measured voltage on electrodes.

### *C. Comparison With Experimental Data*

A 3-D EIT imaging system has been developed at Duke University [24]. The system has a funnel-shaped applicator as shown in Fig. 10(a). The applicator has 128 electrodes attached to it. A detail descriptions and operations of the system can be found in [24]. In each experimental setup, the applicator is filled with saline solution. A small current is injected through a set of predefined electrode pairs sequentially. The voltages between a selected reference electrode and all the other electrodes are measured. Two sets of data are measured in each experiment setups. The first set of data is obtained with only the saline solution and the second set is measured when a phantom is placed in the applicator. In this section, the measured data is used to compare with the simulated data obtained by the SEM forward solver.

The mesh that we used to simulate the system is shown in Fig. 10(b). The mesh has 4448 nodes and 3472 hexahedral elements. The contact impedance of each electrodes varies whenever a new saline solution is poured into the applicator, therefore, we employed a simple least square fitting method to estimate the background conductivity and contact impedances for all the electrodes. In one of the experimental setups, the background conductivity estimated is 0.0043 S/cm. The contact impedances estimated are shown in Fig. 11(a), ranging approximately from 16 to 22 $\Omega \cdot \mathrm{cm}^2$.

We stack all the measurement values into one vector and plot it in a graph. The comparison is shown in Fig. 11(b). Here, only the first 512 values are shown for clarity. The SEM results agree very well with the measured data. The $L_2$ error for the two is less than 0.01. This again validated the accuracy of the SEM forward solver.

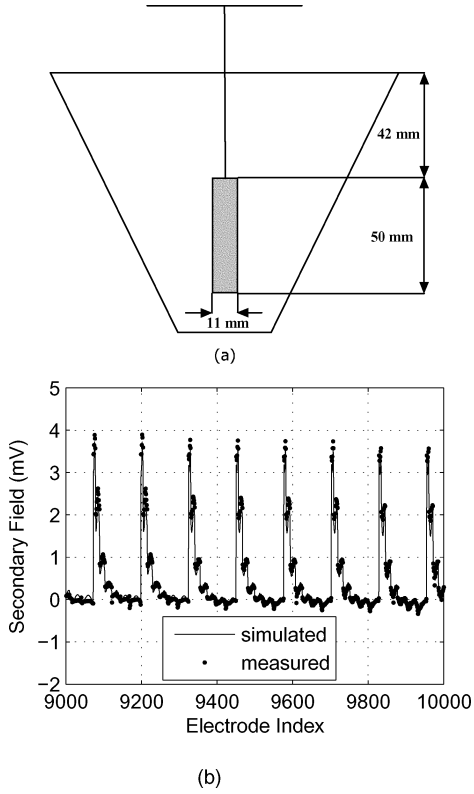


Fig. 12. (a) Conductive, cylindrical object hung in the applicator. (b) Secondary field.

The main objective of EIT is to reconstruct objects that are present in the applicator from the voltage data measured on the electrodes. The difference in voltage measurements between with and without the objects is defined as the secondary field. The secondary field is basically caused by the objects. So, it is essential that the forward model is able to simulate the secondary field accurately.

To verify the accuracy of the SEM forward solver for the secondary field, a metallic cylinder is hung in the middle of the applicator as shown in Fig. 12(a). The experiment is carried out by measuring the voltages on the electrodes without and with the object. The secondary field is simply the difference between the voltages measured with and without the object. The comparison between the measured and simulated secondary field is shown in Fig. 12(b). We observe that the simulated secondary field agree well with the measured data with $L_2$ error of about 0.1.

## IV. Conclusion

The spectral element method has been developed and validated for the EIT forward problem. Numerical results show that SEM is able to achieve the spectral accuracy. The convergence is faster for a larger contact impedance. The improvements in computation time and memory usage for SEM over the first order FEM have been illustrated. Given the same accuracy, the total computational time and memory usage for SEM are much less than the first order FEM. The accuracy of the SEM forward solver has also been validated with experimental data. In summary, we have shown that SEM is an efficient forward solver for electrical impedance tomography. The efficiency of SEM forward solver can be further improved by multigrid techniques such as algebraic multigrid method [25].

## Acknowledgment

The authors would like to thank Dr. G. Shi, K. McCarter, Prof. W. Joines, R. George, and G. Ybarra for their involvement in the hardware development of the 3-D EIT system (separately reported) for collecting the data used in the experimental comparison.

## References

[1] B. Brown, "Medical impedance tomography and process impedance tomography: A brief review," *Meas. Sci. Technol.*, vol. 12, pp. 991–996, 2001.

[2] B. Eyuboglu, B. Brown, and D. Barber, "*In vivo* imaging of cardiac related impedance changes," *IEEE Eng. Med. Biol. Mag.*, vol. 8, no. 1, pp. 39–45, Mar. 1989.

[3] N. Harris, B. Brown, and D. Barber, "Continuous monitoring of lung ventilation with electrical impedance tomography," *Med. Biol. Soc.*, pp. 1754–1755, 1992.

[4] N. Polydorides and W. Lionheart, "A MATLAB based toolkit for three dimensional electrical impedance tomography: A contribution to the eidors project," *Meas. Sci. Technol.*, vol. 13, no. 12, pp. 1871–1883, 2002.

[5] T. Tidswell, A. Gibson, and R. Bayford, "Three-dimensional electrical impedance tomography of human brain activity," *Neuroimage*, vol. 13, no. 2, pp. 283–294, 2001.

[6] S. J. Earl, "Estimation of subsurface electrical resistivity values in 3-D," Ph.D. dissertation, Univ. Bristol, Bristol, U.K., 1998.

[7] M. Loke and R. Barker, "Rapid least squares inversion of apparent resistivity pseudosections by a quasi-Newton method," *Geophys. Prospect.*, vol. 44, pp. 131–152, 1996.

[8] M. Beck and R. Williams, "Process tomography: A European innovation and its applications," *Meas. Sci. Technol.*, vol. 7, pp. 215–224, 1996.

[9] F. Dickin and M. Wang, "Electrical resistance tomography for process tomography," *Meas. Sci. Tech.*, vol. 7, pp. 247–260, 1996.

[10] P. Pinheiro, W. Loh, M. Wang, R. Mann, and R. Waterfall, "Three-dimensional ERT in a stirred mixing vessel," *Comm. Chem. Eng.*, vol. 175, pp. 25–38, 1999.

[11] M. Wang, F. Dickin, and R. Williams, "Modeling and analysis of electrically conductiong vessels and pipelines in electrical-resistance process tomography," *Inst. Elect. Eng. Proc. Sci. Meas. Technol.*, vol. 142, no. 4, pp. 313–322, 1995.

[12] M. Vauhkonen, D. Vadasz, P. Karjalainen, E. Somersalo, and J. Kaipio, "Tikhonov regularization and prior information in electrical impedance tomography," *IEEE Trans. Med. Eng.*, vol. 17, no. 2, pp. 285–293, Apr. 1998.

[13] W. Lionheart, "EIT reconstruction algorithms: Pitfalls, challenges and recent developments," *Physiol. Meas.*, vol. 25, pp. 125–142, 2004.

[14] K. Cheng, D. Isaacson, J. Newell, and D. Gisser, "Electrode models for electrical current computed tomography," *IEEE Trans. Biomed. Eng.*, vol. 36, no. 9, pp. 918–924, Sep. 1989.

[15] K. Paulson, W. Breckon, and M. Pidcock, "Electrode modelling in electrical impedance tomography," *SIAM J. Appl. Math.*, vol. 52, pp. 1012–1022, 1992.

[16] E. Somersalo, M. Cheney, and D. Issacson, "Existence and uniqueness for electrode models for electric current computed tomography," *SIAM J. Appl. Math.*, vol. 52, pp. 1023–1040, 1992.

[17] A. Borsic, "Regularization methods for imaging from electrical measurements," Ph.D. dissertation, Oxford Brookes Univ., Oxford, U.K., 2002.

[18] A. Patera, "A spectral-element method for fluid dynamics: Laminar flow in a channel expansion," *J. Comput. Phys.*, vol. 54, pp. 468–488, 1984.

[19] J. H. Lee, T. Xiao, and Q. H. Liu, "A 3-D spectral-element method using mixed-order curl conforming vector basis functions for electromagnetic fields," *IEEE Trans. Microw. Theory Tech.*, vol. 12, no. 1, pp. 1848–1858, Jan. 2005.

[20] C. Canuto, M. Hussaini, A. Quarteroni, and T. Zang, *Spectral Methods in Fluid Dynamics*. Berlin, Germany: Springer-Verlag, 1988.

[21] B. Fornberg, *A Practical Guide to Pseudospectral Methods*. Cambridge, U.K.: Cambridge Univ. Press, 1998.

[22] R. Peyret, *Spectral Methods for Incompressible Viscous Flow*. Berlin, Germany: Springer-Verlag, 2002.

[23] J. H. Lee and Q. H. Liu, "An efficient 3-D spectral-element method for schrodinger equation in nanodevice simulation," *IEEE Trans. Comput.-Aided Design Integr. Circuits Syst.*, vol. 24, no. 12, pp. 1848–1858, Dec. 2005.

[24] G. Ye, K. Lim, R. George, G. Ybarra, W. Joines, and Q. H. Liu, "3-D EIT for breast cancer imaging: System design and measurements," in *Proc. 3rd Int. Symp. Biomed. Imag.: Macro to Nano*, 2006, pp. 1092–1095.

[25] M. Soleimani, C. Powell, and N. Polydorides, "Improving the forward solver for the complete electrode model in EIT using algebraic multigrid," *IEEE Trans. Med. Imag.*, vol. 24, no. 5, pp. 577–583, May 2005.